🔴 Check for updates

Structural and ethylene oligomerization studies of chelating (imino)phenol Fe(II), Co(II) and Ni(II) complexes: an experimental and theoretical approach†

Makhosonke Ngcobo,[a] Holliness Nose,[b] Arumugam Jayamani[a] and Stephen O. Ojwach ⓘD *[a]

The metal complexes [Fe(**L1**)$_2$] (**Fe1**); [Fe(**L2**)$_2$] (**Fe2**); [Fe(**L3**)$_2$] (**Fe3**); [Co(**L1**)$_2$] (**Co1**); [Co(**L2**)$_2$] (**Co2**); [Co(**L3**)$_3$] (**Co3**); [Ni(**L1**)$_2$] (**Ni1**); [Ni(**L2**)$_2$] (**Ni2**) and [Ni(**L3**)$_3$] (**Ni3**); where L = 2,4-dibromo-6-((pyridin-2-ylimino)methyl)phenol (**L1H**), 2,4-dibromo-6-(((4-methylpyridin-2-yl)imino)methyl)phenol (**L2H**) and 2,4-dibromo-6-((quinolin-8-ylimino)methyl)phenol (**L3H**), were synthesized in good yields. The complexes were characterized using IR spectroscopy, UV-visible spectroscopy, mass spectrometry, magnetic moment measurements, elemental analysis, and X-ray crystallography. The molecular structures of complexes **Fe3a** (oxidised form of **Fe3**) and **Ni3** confirmed the isolation of bis(chelated) tridentate bound octahedral compounds. Activation of the complexes with the EtAlCl$_2$ co-catalyst produced active catalysts in the ethylene oligomerization reactions to afford mainly C$_4$ and C$_6$ oligomers. The catalytic activities and product distribution were largely controlled by the nature of the ligand and the metal atom. Density functional theory calculations were used to investigate the influence of complex properties and global descriptors in the ethylene oligomerization reactions. The stability and magnitude of the charge of the metal atom appear to drive the overall catalytic activities of the complexes.

1. Introduction

Ethylene oligomerization reactions are major industrial processes, producing tonnes of olefins which are raw materials extensively used in the production of detergents, lubricants, plasticizers and polyolefins among others.[1–4] In the matrix of olefin production, late transition metal catalysts have shown high catalytic activities and selectivities, as well as tolerance to polar monomers, compared to early transition metal counterparts.[5] As a result, the past decades have witnessed significant progress in the use of late transition metal complexes as ethylene oligomerization catalysts.[6,7] For example, Ni(II) complexes are currently applied industrially in the

[a] School of Chemistry and Physics, University of KwaZulu-Natal, Private Bag X01, Scottsville, Pietermaritzburg 3209, South Africa. E-mail: ojwach@ukzn.ac.za

[b] School of Chemistry and Material Science, Technical University of Kenya, Haile Selasie Avenue, P.O. Box 52428-00200, Nairobi, Kenya

† Electronic supplementary information (ESI) available: Additional spectroscopy and mass spectral data (NMR, FT-IR and LC–MS spectroscopy, GC and GC–MS) in addition to these catalysis data. Crystallographic data of compounds **Fe3a** and **Ni3** in this article can be accessed *via* Cambridge Crystallographic Data Centre respectively. CCDC 2126949 (**Fe3a**) and 2126951 (**Ni3**). For ESI and crystallographic data in CIF or other electronic format see DOI: 10.1039/d1nj06065a

Shell Higher Olefin Process (SHOP).[8] The pioneering work of Brookhart *et al.*[9] on the application of α-diimine nickel(II) complexes in olefin oligomerization and polymerization reactions has stimulated the development of new modified Ni(II) complexes based on nitrogen-donor ligands with varied outcomes.[10–15]

Other late transition metal catalysts, most notably, Fe(II) and Co(II) systems ligated on nitrogen-donor ligands, independently discovered by Brookhart and Gibson are also known for their high catalytic activities and selectivity towards the formation of linear and branched polyethylenes.[16,17] Subsequent research studies have thus focused on modifying these catalyst models to achieve a balance between the catalytic activity, selectivity and stability.[18–22] Schiff base ligands display interesting and varied coordination chemistries and, consequently, have attracted much attention in the design of ethylene polymerization and oligomerization catalysts.[23–25] For example, the use of bidentate salicylaldehyde ligands and their derivatives with late transition complexes has led to the development of active and selective ethylene oligomerization catalysts.[26,27]

We recently reported the use of Fe(II) and Co(II) complexes bearing 2-[(ethylimino)methyl]phenol ligands as catalysts in ethylene oligomerization reactions.[28,29] Driven by their promising

catalytic performances, we hereby report on the syntheses and structural elucidation of Fe(II), Co(II) and Ni(II) complexes of bromo-substituted salicylaldimine ligands and investigate their potential as catalysts in ethylene oligomerization reactions. Density Functional theory studies were performed to gain insight into the effect of the complex structure and other global descriptors on the catalytic behaviour of these complexes and are herein discussed.

2. Experimental section

2.1. Materials and instrumentation

All solvents were of analytical grade and were dried and distilled prior to use. The reagents 3,5-dibromosalicylaldehyde (98%), 2-aminopyridine (99%), 2-amino-4-methylpyridine (99%) and 8-aminoquinoline (98%) were purchased from Sigma-Aldrich; anhydrous $CoCl_2$ (98%), $FeCl_2 \cdot 4H_2O$ (98%) and [$NiBr_2(DME)$] (DME = ethylene glycol dimethyl ether) (97%) were purchased from Merck and used as received without further purification. The synthetic protocols and spectral data of the (imino)phenol ligands (**L1H-L3H**) are given in the ESI.† The infrared spectra were recorded on a PerkinElmer Spectrum 100 in the 4000–400 cm^{-1} range. ESI-mass spectra were recorded on an LC premier micro mass spectrometer. The magnetic moments were determined using an Evans balance (Sherwood MK-1). The ultraviolet absorption spectra of the metal complexes were recorded using a PerkinElmer LAMBDA 35 spectrometer (2002). The scanning region is from 150–700 nm and the spectral bandwidth is 1 nm. GC analyses were performed on a Varian CP-3800 gas chromatograph equipped with a flame ionization detector and a 30 m (0.2 mm i.d., 0.25 μm film thickness) CP-Sil5 CB capillary column.

2.2. Synthesis of Fe(II), Co(II) and Ni(II) complexes

2.2.1. Synthesis of [Fe(L1)₂] (Fe1). To a solution of anhydrous $FeCl_2$ (0.06 g, 0.50 mmol) in methanol (10 mL), ligand **L1H** (0.34 g, 1.00 mmol) dissolved in methanol (10 mL) was added dropwise and stirred overnight at room temperature. The black precipitate formed was filtered, washed with ethanol, methanol, and ether and dried to obtain a dark brown powder. Yield: 0.30 g (71%). TOF ESI-MS: m/z (%) 760 [M, 10%].$^+$ IR ν_{max}/cm^{-1}: 3063 (ν_{OH}), 1613 ($\nu_{C=N}$); μ_{obs} = 5.60 BM. Anal. calcd for $C_{24}H_{14}Br_4FeN_4O_2$: C, 37.49; H, 1.84; N, 7.29. Found (%): C, 37.85; H, 1.76, N, 7.19.

Complexes **Fe2, Fe3, Co1, Co2,** and **Co3** and **Ni1, Ni2** and **Ni3** were synthesized following the procedure described for complex **Fe1**.

2.2.2. Synthesis of [Co(L1)₂] (Co1). Anhydrous $CoCl_2$ (0.06 g, 0.50 mmol) and ligand **L1H** (0.36 g, 1.00 mmol) were used. Blue solid. Yield: 0.28 g (65%); TOF ESI-MS: m/z (%) 769.78 [M, 10%]$^+$; IR ν_{max}/cm^{-1}: 3063 (ν_{OH}), 1623 ($\nu_{C=N}$); μ_{obs} = 3.26 BM. Anal. calcd for $C_{24}H_{14}Br_4CoN_4O_2$: C, 37.64; H, 1.84; N, 7.32. Found (%): C, 37.32, H, 1.56; N, 7.58.

2.2.3. Synthesis of [Ni(L1)₂] (Ni1). [$NiBr_2(DME)$] (0.16 g, 0.50 mmol) and ligand **L1H** (0.36 g, 1.00 mmol) were used.

Green solid. Yield: 0.44 g (84%). TOF ESI-MS: m/z (%) 763 [Ni(**L1**)₂, 15%]$^+$; IR ν_{max}/cm^{-1}: 3288 (ν_{OH}), 1634 ($\nu_{C=N}$); μ_{obs} = 2.82 BM. Anal. calcd for $C_{24}H_{14}Br_4NiN_4O_2$: C 37.50; H, 1.84; N, 7.64. Found (%): C 37.49, H 1.54, N 7.94.

2.2.4. Synthesis of [Fe(L2)₂] (Fe2). Anhydrous $FeCl_2$ (0.07 g, 0.50 mmol) and ligand **L2H** (0.37 g, 1.00 mmol) were used. Dark brown solid. Yield: 0.32 g (72%); TOF ESI-MS: m/z (%) 793.77 [Fe(**L2**)₂, 14%]$^+$; IR ν_{max}/cm^{-1}: 3063 (ν_{OH}), 1609 ($\nu_{C=N}$); μ_{obs} = 5.15 BM. Anal. calcd for $C_{26}H_{18}Br_4FeN_4O_2$: C, 39.33; H, 2.29; N, 7.06. Found (%): C 39.22, H, 2.36, N 7.09.

2.2.5. Synthesis of [Co(L2)₂] (Co2). Anhydrous $CoCl_2$ (0.06 g, 0.5 mmol) and ligand **L2H** (0.37 g, 1.00 mmol) were used. Blue solid. Yield: 0.29 g (68%); ESI-MS: m/z (%) 819.74 [Co(**L2**)₂ + Na, 22%]$^+$; IR ν_{max}/cm^{-1}: 1613 ($\nu_{C=N}$); μ_{obs} = 3.99 BM. Anal. calcd for $C_{26}H_{18}Br_4CoN_4O_2$: C, 39.18; H, 2.28; N, 7.03. Found (%): C, 38.98, H, 2.60; N, 7.00.

2.2.6. Synthesis of [Ni(L2)₂] (Ni2). [$NiBr_2(DME)$] (0.16 g, 0.50 mmol) and ligand **L2H** (0.37 g, 1.00 mmol) were used. Green solid. Yield: 0.39 g (78%); TOF ESI-MS: m/z (%) 818.87 [M + Na, 42%]$^+$; IR ν_{max}/cm^{-1}: 3063 (ν_{OH}), 1623 ($\nu_{C=N}$); μ_{obs} = 3.05 BM. Anal. calcd for $C_{26}H_{18}Br_4NiN_4O_2$: C, 39.13; H, 2.28; N, 7.03. Found (%): C, 38.92; H, 2.66; N, 6.92.

2.2.7. Synthesis of [Fe(L3)₂] (Fe3). Anhydrous $FeCl_2$ (0.07 g, 0.50 mmol) and ligand **L3H** (0.40 g, 1.00 mmol) were used. Green solid. Yield: 0.35 g (73%); TOF ESI-MS: m/z 890 [Fe(**L3**)₂ + (2H + Na), 10%]$^+$; IR ν_{max}/cm^{-1}: 1614 ($\nu_{C=N}$); μ_{obs} = 5.43 BM. Anal. calcd for $C_{32}H_{18}Br_4FeN_4O_2$: C, 44.38; H, 2.10; N, 6.47. Found (%): C, 44.52; H, 2.13; N, 6.59. Recrystallization of the complex in methanol solvent by a slow evaporation afforded green single crystals suitable for X-ray analyses.

2.2.8. Synthesis of [Co(L3)₂] (Co3). Anhydrous $CoCl_2$ (0.06 g, 0.5 mmol) and ligand **L3H** (0.40 g, 1.00 mmol) were used. Blue solid. Yield: 0.33 g (72%); TOF ESI-MS: m/z 868.87 [Co(**L3**)₂, 100%]$^+$; IR ν_{max}/cm^{-1}: 1619 ($\nu_{C=N}$); μ_{obs} = 3.59 BM. Anal. calcd for $C_{16}H_{10}Br_2Cl_2CoN_2O$: C, 35.86; H, 1.88; N, 5.23. Found (%): C, 35.82; H, 1.66; N, 5.29.

2.2.9. Synthesis of [Ni(L3)₂] (Ni3). $NiBr_2(DME)$ (0.16 g, 0.50 mmol) and ligand **L3H** (0.40 g, 1.00 mmol) were used. Green solid. Yield: 0.42 g (75%); TOF ESI-MS: m/z (%) 890.79 [M + Na, 2%]$^+$; IR ν_{max}/cm^{-1}: 1635 ($\nu_{C=N}$), 572 (ν_{Ni-O}); μ_{obs} = 2.78 BM. Anal. calcd for $C_{32}H_{18}Br_4NiN_4O_2$: C, 44.24; H, 2.09; N, 6.45. Found (%): C, 43.82; H, 2. 66; N, 6.29. Recrystallization of the complex in methanol solvent by slow evaporation afforded green single crystals suitable for X-ray analyses.

2.3. X-ray crystallography data collection

Single orange block-shaped crystals of **Fe3a** and green rod-shaped crystals of **Ni3** were recrystallized from methanol solvent by slow evaporation. A suitable crystal of each complex was selected and mounted on a MITIGEN holder in Paratone oil on a Bruker APEX-II CCD diffractometer. The crystal was kept at T = 100(2) K during data collection. Using **Olex2**,[30] the structure was solved using **ShelXS-2013**[31] structure solution program, using the direct solution method. The model was refined using version 2016/6 of **ShelXL**,[32] using least squares minimisation.

2.4. Density functional theory calculations

All computational calculations were carried out using the Gaussian 16 suite of programs.[33] Density functional theory with Becke's three-parameter hybrid functional (B3),[34,35] for the exchange part and the Lee–Yang–Parr (LYP) correlation function,[36] accepted as a cost-effective approach has been used to compute optimized structural geometrical parameters, energies, natural bond orbitals (NBOs) and UV-vis spectra of the complexes. The LanL2DZ (Los Alamos International 2 Double ζ) basis set was used for the metals throughout the study, and 6-311G(d,p) basis set was used for all other atoms in geometry optimizations, NBO analysis, and excited state calculations. To model the UV-vis spectrum, electronic transitions, vertical excitation energies, absorbance and oscillator strengths of metal complexes, time-dependent density functional theory (TD–DFT) method was performed. The frontier molecular orbital (such as the highest occupied molecular orbital (HOMO) and the lowest unoccupied molecular orbital (LUMO)) energies were determined by the TD–DFT approach.
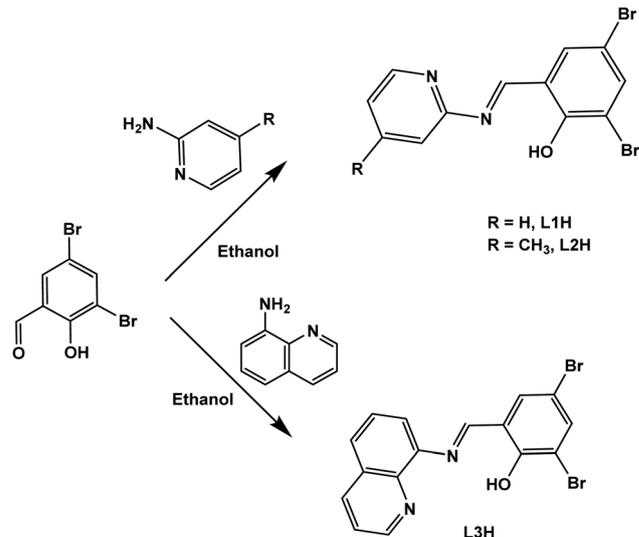
2.5. Ethylene oligomerization experiments

The ethylene oligomerization reactions were carried out utilizing a 100 mL stainless steel reactor equipped with a stirrer bar. A pre-weighed amount of the synthesized pre-catalyst (10.0 μmol) in chlorobenzene (10 mL) was transferred into a dry Schlenk tube *via* a cannula under a nitrogen atmosphere. This was followed by the addition of the respective co-catalyst (EtAlCl$_2$ or MMAO) using a syringe. The resultant solution in the Schlenk tube was then transferred using a cannula into the pre-evacuated reactor, followed by the addition of 20 mL of chlorobenzene or toluene solvent to give a total volume of 30 mL. The reactor was then purged with ethylene gas and pressure and temperature were set at 10 bar and 30 °C, respectively, and the reaction was initiated by switching on the magnetic stirrer for 1 h. Upon completion of the oligomerization process, the reactor was cooled to about 10 °C using liquid nitrogen and the unreacted ethylene was drained. This was followed by quenching the mixture through the addition of 10% HCl (2 mL). Aliquots of the reaction sample were placed in GC-vials and analyzed to determine both the catalytic activity and oligomer compositions. Heptane was used as the internal standard[37] while GC–MS data were used to establish the molecular weights and identities of the oligomer products.

3. Results and discussion

3.1. Synthesis and spectroscopic characterization of pyridine/quinoline (imino)phenol Fe(II), Co(II) and Ni(II) metal complexes

Schiff's base ligands (L1H–L3H) were synthesized in high yields (81–89%) by condensation reactions of stoichiometric amounts of 3,5-dibromo salicylaldehyde with 2-aminopyridine, 4-methyl-2-aminopyridine and 8-aminoquinoline, respectively, as depicted in Scheme 1. The reactions of ligands L1H–L3H with the respective metal salts, FeCl$_2$, CoCl$_2$ or [Ni(DME)Br$_2$] resulted in the

Scheme 1 Syntheses of bromo substituted pyridine and quinolone Schiff base ligands.
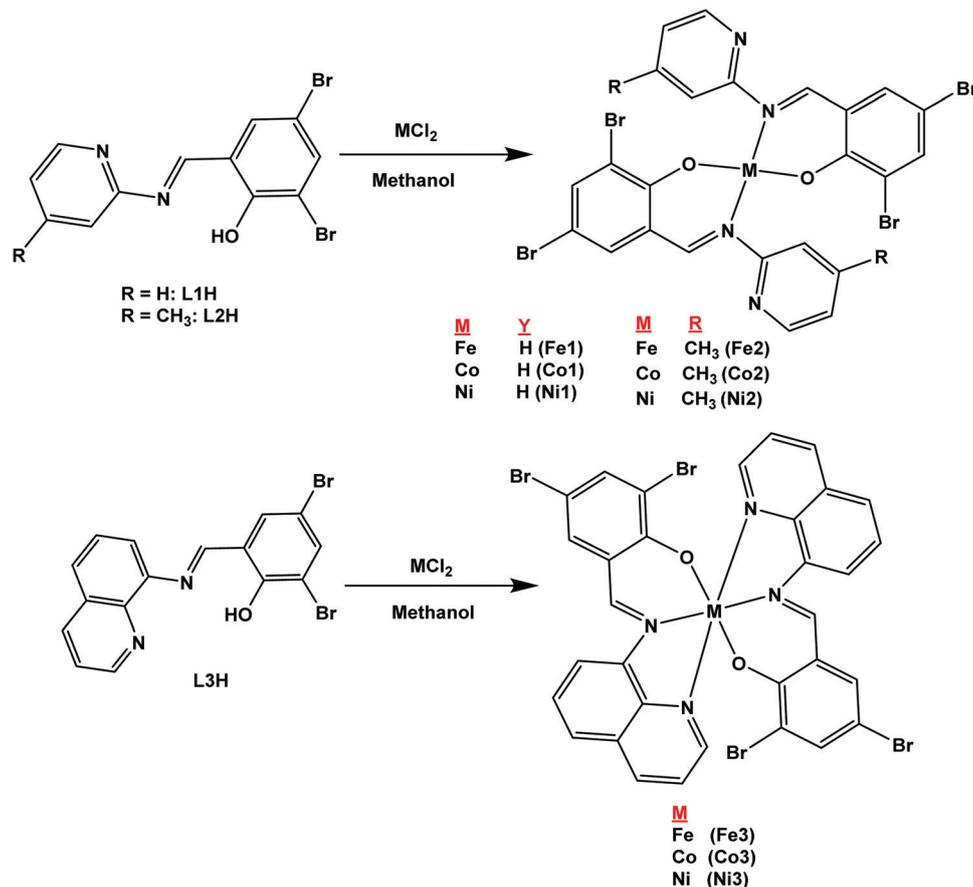
formation of the respective Fe(II), Co(II) and Ni(II) complexes in good to high yields (65%–84%) as shown in Scheme 2.

The compounds were characterized using ^{1}H NMR (Fig. S1–S3, ESI†) ^{13}C NMR (Fig. S4–S6, ESI†) for the ligands, IR spectroscopy (Fig. S7–S18, ESI†), mass spectrometry (Fig. S19–S30, ESI†), elemental analyses, magnetic moment measurements and single crystal X-ray crystallography. IR spectra of complexes Fe(II), Co(II) and Ni(II) showed sharp absorption band characteristic of C=N stretching frequency in the 1609–1617 cm^{-1} region (Fig. S13–S21, ESI†). Notably, the C=N diagnostic absorption band was recorded at lower frequencies for the corresponding ligands, which pointed to the successful complexation of the ligands. Deprotonation of ligands L1H–L3H to form anionic ligands (L1$^-$–L3$^-$) upon coordination was derived from the absence of the OH stretching vibrations in the coordinated ligands. This data is also consistent with the absence of the halides in the metal coordination sphere.[38] For example, the quinoline ligand L3H showed the OH vibration signal at 3062 cm^{-1} (Fig. S9, ESI†), while this signal is absent in the corresponding complexes Fe3, Co3 and Ni3 (Fig. S16–S18, ESI†).

Mass spectrometry was also used in confirmation of the molecular masses and identities of the Fe(II), Co(II) and Ni(II) complexes (Fig. S22–S30, ESI†). From the mass spectral data, the formation of the bis(ligated) complexes could be deduced as depicted in Scheme 2. For instance, ESI mass spectrum of complex Fe1 showed a molecular ion peak at m/z = 764 amu (10%) and agrees with the proposed formula of [Fe(L1)$_2$] and molar mass of 765.85 g mol^{-1} (Fig. S22, ESI†). In addition, there was good agreement between the theoretical and experimental isotopic mass distributions of the complexes (Fig. S22–30, ESI†).

The magnetic moments of complexes Fe1–Fe3 were recorded as 5.60 BM, 5.15 BM and 5.43 BM respectively. These values are notably higher than the spin-only value of 4.90 BM for d^6 Fe(II) complexes at 300 K. Nevertheless, the values fall within the

Scheme 2 Syntheses of pyridine and quinoline (imino)phenol Fe(II), Co(II) and Ni(II) complexes.

expected range of high spin Fe(II) complexes of 5.10–5.70 BM at 300 K.[39] Similarly, values of 3.26 BM, 3.99 BM and 3.59 BM for the Co(II) complexes **Co1–Co3** were recorded respectively, and are comparable to the spin-only value of 3.87 BM for high spin d^7 Co(II) complexes at 300 K. Finally, the magnetic moment values of 2.82 BM, 3.05 BM and 2.78 BM recorded for the Ni(II) complexes **Ni1–Ni3** respectively, were consistent with spin-only value of 2.83 BM and fall within the expected range of 2.90 BM–4.20 BM at 300 K for high-spin d^8 Ni(II) complexes.[40] One interesting import from the magnetic moments data is that the Fe(II) complexes showed relatively high observed magnetic moments, pointing to larger crystal field effects (orbital contribution) for the Fe(II) complexes in comparison to the Co(II) and Ni(II) complexes.[41] The micro-analyses data of the complexes were consistent with two ligand motifs per metal atom, as illustrated in Scheme 2 and confirmed the purity of the bulk materials.

3.2. Molecular structures of complexes Fe3a and Ni3

Single crystals suitable for X-ray analyses of complexes **Fe3** and **Ni3** were obtained by slow evaporation of their methanol solutions at room temperature. The resolved molecular structure of complex **Fe3**, however, contains an Fe(III) metal center with a Br⁻ counter anion, and two anionic ligand **L3⁻** units (**Fe3a**), pointing to *in situ* oxidation during crystallization

(Fig. 1). Oxidation of Fe(II) to Fe(III) complexes is common, and has been associated with the presence of trace amounts of air or moisture.[42–44] Table S1 (ESI†) gives a summary of the crystallographic data and structure refinement parameters,
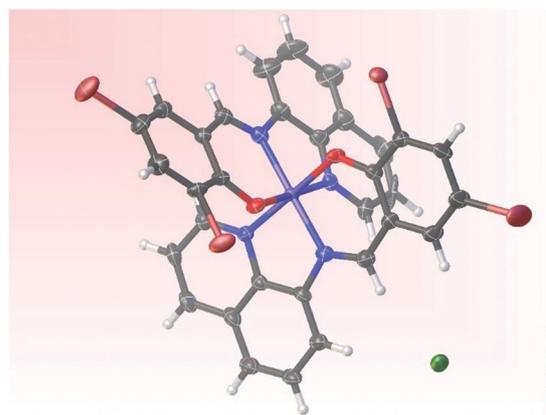

Fig. 1 Molecular structure of complex **Fe3a**. Ellipsoids are illustrated at 50% probability. Selected bond lengths (Å) and angles (°): Fe(1)-N(5), 1.897(5); Fe(1)-N(4), 1.931(5); Fe(1)-N(3), 1.955(5); Fe(1)-N(1), 1.912(5); Fe(1)-O(2), 1.885(4); Fe(1)-O(3), 1.881(4); O(3)-Fe(1)-N(4), 178.2(2); O(2)-Fe(1)-N(3), 178.6(2); O(2)-Fe(1)-O(3), 88.97(18); O(2)-Fe(1)-N(5), 88.27(18); O(3)-Fe(1)-N(5), 95.64(18); N(3)-Fe(1)-N(5), 91.9(2); N(1)-Fe(1)-N(5), 175.3(2); N(4)-Fe(1)-N(5), 84.6(2).
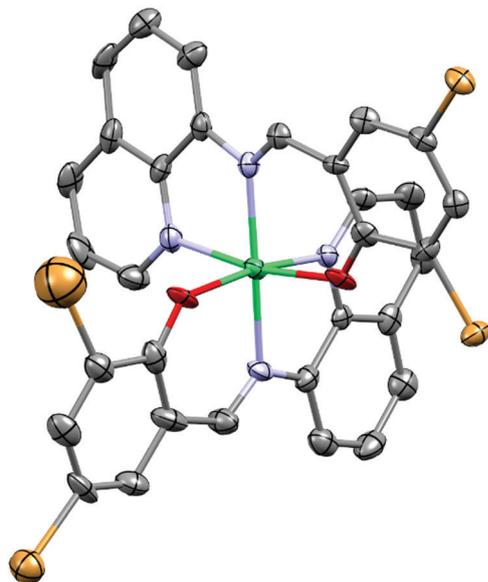
Fig. 2 Molecular structure of complex **Ni3** with atoms shown as 30% thermal ellipsoids, hydrogen atoms are removed for more clarity. Selected bond lengths (Å) and angles (°): Ni(1)-O(2), 2.039(7); Ni(1)-N2(2), 2.069(8); Ni(1)-N(1), 2.088(8); Ni(1)-N(3), 2.112(8); Ni(1)-N(4), 2.047(8); Ni(1)-O(1), 2.088(7); O(1)-Ni(1)-N(1), 171.2(3); O(2)-Ni(1)-N(3), 169.7(3); N(4)-Ni(1)-N(2), 174.0(3); N(2)-Ni(1)-O(1), 91.0(3); N(2)-Ni(1)-N(1), 80.2(3); N(4)-Ni(1)-O(1), 92.9(3); and N(4)-Ni(1)-N(1), 95.8(3).

while Fig. 1 and 2 represent molecular structures and selected bond parameters for complexes **Fe3a** and **Ni3** respectively. The molecular structures of complexes **Fe3a** and **Ni3** confirm the presence of bis(chelated) mononuclear complexes in which the two tridentate N^N^O anionic ligand ($L3^-$) lie perpendicular to each other around the metal centre. The crystal structures of the complexes **Fe3a** and **Ni3** exhibit two five- and two six-membered chelate rings occupying meridional positions of the octahedral structures.[45] The four coordinating atoms that make up the basal plane are the two phenoxy–O atoms and two quinoline-N atoms, while the axial sites are occupied by the two imine N-donor atoms.

The average $Ni–N_{quinoline}$ bond distance of 2.0795 Å of complex **Ni3** is longer than the mean $Ni–N_{imine}$ bond distance of 2.0785 Å. In a related study, Insiti *et al.*[46] reported a $Ni–N_{quinoline}$ bond length of 2.097 Å for the bis(4-bromo-2-(((quinolin-8-)imino)methyl)phenolato)-Ni(II) complex, which is 0.0175 Å longer than the mean $Ni–N_{quinoline}$ bond length of 2.0795 Å for complex **Ni3**. In addition, the mean $Ni–N_{quinoline}$ (2.0795 Å) and $Ni–N_{imine}$ (2.0785 Å) bond distances obtained for compound **Ni3** are longer than the mean bond lengths of 2.104 ± 0.027 Å and 2.055 ± 0.060 Å reported in 47 and 51 similar structures respectively.[47] The average $Ni–O_{phenolic}$ bond length of 2.0635 Å is shorter than the average bond length of 2.024 ± 0.026 Å calculated for 64 similar structures.[47] It is also noteworthy to mention that the reported $Ni–N_{quinoline}$ (2.0795 Å), $Ni–N_{imine}$ (2.0785 Å) and the $Ni–O_{phenolic}$ (2.0635 Å) mean bond lengths all lie within the reported minimum and maximum bond distances of 2.044 Å–2.182 Å, 1.977 Å–2.239 Å and

1.956 Å–2.092 Å, reported in 47, 51 and 64 similar structures, respectively.[48] For complex **Fe3a**, the average $Fe–N_{imine}$ bond distance of 1.926 Å, is slightly longer than the average $Fe–N_{quinoline}$ bond length of 1.9216 Å. In addition, the average $Fe–N_{quinoline}$, $Fe–N_{imine}$ and $Fe–O_{phenolic}$ bond lengths of 1.9216 Å, 1.926 Å and 1.883 Å are all shorter than the mean $Fe–N_{quinoline}$, $Fe–N_{imine}$ and $Fe–O_{phenolic}$ bond lengths of 2.036 ± 0.085 Å, 2.066 ± 0.087 Å and 1.905 ± 0.037 Å respectively, reported for 396, 323 and 453 similar structures respectively.[48] More significantly, it appears that since the reported mean $Fe–N_{imine}$ bond distance of 1.926 Å has been the shortest reported to date, the minimum $Fe–N_{imine}$ bond length calculated from 323 similar structures is 1.933 Å.[48]

The bond angles for O(3)-Fe(1)-N(4), O(2)-Fe(1)-N(3), and N(1)-Fe(1)-N(5) of 175.3(2)°, 178.6(2)° and 178.2(2)°, respectively, in complex **Fe3a** and the bond angles for O(1)-Ni(1)-N(1), O(2)-Ni(1)-N(3), and N(4)-Ni(1)-N(2) of 171.2(3)°, 169.7(3)° and 174.0(3)°, respectively in complex **Ni3** deviate from the expected 180° linear geometry by 2–11,° revealing distorted octahedral geometries. For example, the average N^N five-membered bite angles in complexes **Fe3a** and **Ni3** were calculated to be 88.25° and 88.0° respectively, while the mean N^O six-membered bite angle was found to be 91.55° in both cases. In addition, the packing of **Ni3** was observed to be stabilized by edge-to-edge π···π stacking, Br···H, C–H···π and nonconventional C–H···O hydrogen bonding interactions. In contrast to the crystal structure of the **Ni3** complex, no hydrogen bonding interactions and structure stabilizations could be quantified for the Fe(II) complex **Fe3a**.

3.3. Experimental and theoretical UV-visible spectral analyses

The electron transfer from bonding or nonbonding orbitals to antibonding orbitals induces electronic absorption behaviour in the Fe(II), Co(II), and Ni(II) metal complexes. In general, $π →$ $π^*$, $n → π^*$, $n → σ^*$, d → d, and L ↔ M transitions are possible in metal–organic materials.[49–51] In this study, the absorption UV spectrum of the metal compounds was calculated by the TD–DFT method using the LanL2DZ basis set for metal ions and 6-311G (d,p) basis set for all other atoms. The computed wavelength of absorption ($λ$), the value of oscillator strength (f), excitation energy (E), transition assignments and the predominant transitions along with the experimental UV data are listed in Table 1 and Fig. S2, S3 (ESI†). The calculated wavelengths are also plotted against the oscillator strengths using a Gaussian line shape as shown for complex **Co1** in Fig. 3 and Fig. S31 (ESI†) for the remaining complexes. Table S3 (ESI†) shows the HOMO/LUMO diagrams, corresponding to the peaks displayed in the spectra of the metal complexes calculated using the B3LYP density functional theory (DFT) as shown in Table S2 (ESI†). The calculated UV spectrum of the **Co1** complex shows four electronic transitions at 404, 310, 244, and 201 nm, corresponding to experimental values at 402, 298, 271, and 232 nm as shown in Table 1. The electronic transitions observed are assigned as follows: 402 nm is due to d → d transitions, 298 nm is due to $n → π^*$ transitions, 271 nm is due to $π → π^*$ transitions and 232 nm and are due to $n → σ^*$

Table 1 Theoretical and experimental electronic transitions, oscillator strengths and assignments of the metal complexes

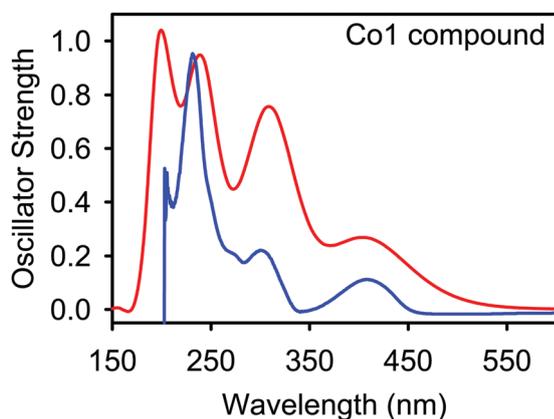| B3LYP/6-311G(d,p)				Experimental	
Metal compound	λ (nm)	(f)	E (eV)	λ (nm)	Assignments
Fe1	392	0.0843	3.1632	—	d → d
	305	0.3037	4.0695	302	n → π*
	234	0.1967	5.2927	259	π → π*
	197	0.1948	6.2847	232	n → σ*
Co1	404	0.1174	3.0677	402	d → d
	310	0.2124	3.9940	298	n → π*
	244	0.2457	5.0901	271	π → π*
	201	0.1716	6.1662	232	n → σ*
Ni1	409	0.0964	3.0293	414	d → d
	294	0.2178	4.2121	297	n → π*
	237	0.0882	5.2234	269	π → π*
	198	0.1338	6.2652	234	n → σ*

Fig. 3 Absorption spectra of **Co1** compound. The red curve shows the absorption spectra generated theoretically by using B3LYP functional whereas the blue curve shows the absorption spectra generated experimentally.

transitions. These bands were also consistent with high-spin distorted tetrahedral complexes of ligands **L1** and **L2**.[52]

The low intensity band at 402 nm is consistent with the d → d transitions of the metal cation. However, the major contributor to this metal compound involved pure π → π* excitations within the aromatic rings. This is followed by intra-ligand n → π* transitions that may occur by nitrogen, oxygen and Br atom lone pair electrons. Small transitions involving n → σ* transitions are also observed during excitation. A comparison between B3LYP theoretically determined wavelength values and experimentally determined wavelength values showed good agreements. A similar trend was observed for the remaining metal complexes, as shown in the supporting information, Table S2 and Fig. S31 (ESI†). In all the cases, the experimental and theoretical UV-vis spectra of the M^{2+} complexes agree, confirming that the complexes exist as M^{2+} in the bulk state. It is therefore reasonable to assert that the crystal structure of **Fe3a** (obtained from a solution of **Fe3**), which has a Fe^{3+} metal atom (Fig. 1), was formed *via* an *in situ* oxidation process during crystallization.

3.4. Ethylene oligomerization reactions catalyzed by the Fe(II), Co(II) and Ni(II) complexes

3.4.1 Preliminary investigation and optimization studies. Having gained insights into the coordination chemistry of the metal complexes, we then shifted our focus on the study of their behaviour as catalyst precursors in ethylene oligomerization reactions. The complexes were investigated using MMAO-12 and $EtAlCl_2$ as activators in toluene and chlorobenzene respectively. Activation with MMAO-12 in toluene solvent resulted in inactive species in ethylene oligomerization reactions (Fig. S32, ESI†).[53,54] On the other hand, activation with the $EtAlCl_2$ co-catalyst in toluene medium mainly produced alkylated products (Table S4 and Fig. S33, ESI†).[55] Thus the complexes were activated with the $EtAlCl_2$ co-catalyst in the chlorobenzene solvent to avoid the formation of Friedel–Crafts alkylated products. In chlorobenzene solvent, the complexes displayed high catalytic activities to the tune of 1608 kg mol^{-1} h^{-1}, mainly producing butenes and hexenes as confirmed from GC and GC-MS spectral data (Fig. S34, ESI†). The optimum reaction conditions in the oligomerization of ethylene reactions were performed using the **Ni1**/$EtAlCl_2$ system by varying the Al/Ni ratio, time, pressure and temperature conditions (Table S4, ESI†). The optimized reactions conditions were obtained as follows: temperature, 30 °C; time, 1 h; Al/Ni, 250; and pressure of 10 bar (Table S4, ESI† entry 4).

3.4.2. The effect of the structures of complexes on the catalytic performance of the complexes. After establishing the optimized reactions in the ethylene oligomerization reactions using complex **Ni1**, we then studied the influence of complex structure (ligand and metal identity) as given in Table 2. Evidently, the identity of the metal centre played a significant role in controlling the catalytic activity of the complexes. In general Ni(II) complexes were more active than their respective Fe(II) and Co(II) analogues. For example, catalytic activity of 1608 kg mol^{-1} h^{-1} was obtained for the **Ni1** complex, while its analogous complexes **Fe1** and **Co1** afforded catalytic activities of 918 kg mol^{-1} h^{-1} and 1036 kg mol^{-1} h^{-1} respectively (Table 2, entries 1–3), consistent with the literature findings.[23,56,57]

The steric and electronic properties of the coordinated ligands also played a crucial role in controlling the catalytic activity of the complexes. For example, comparisons of complexes supported on the aldimine ligand **L1H** (**Fe1**, **Co1** and **Ni1**) with their counterparts (**Fe2**, **Co2** and **Ni2**) supported on the ketimine ligand **L2⁻**, revealed that introduction of the methyl substituent in the pyridyl ring reduced the catalytic activities of the complexes. For example, complex **Fe1** displayed catalytic activity of 918 kg mol^{-1} h^{-1} whilst its analogous complex **Fe2**, showed lower catalytic activities of 865 kg mol^{-1} h^{-1} (Table 2, entries 1 and 4). This trend may be attributed to electronic factors, where the unsubstituted complex **Fe1** results in a more electropositive Fe(II) metal centre, than its methyl substituted counterpart **Fe2**.[58]

Furthermore, the catalytic activities of the complexes were compromised when the pyridyl ring in complexes **Fe1**, **Co1** and **Ni1** was changed to the quinoline group as in complexes **Fe3**, **Co3** and **Ni3**. For example, complex **Fe3** displayed a lower

Table 2 Ethylene oligomerization data catalyzed by Fe(II), Co(II), and Ni(II) complexes[a]

Entry	Catalyst	Yield[b] (g)	Activity (kg mol^{-1} h^{-1})	Product distribution (%)[c]	
				C$_4$ (α-C$_4$)	C$_6$ (α-C$_6$)
1	**Fe1**	9.18	918	39 (92)	61 (14)
2	**Co1**	10.36	1036	48 (95)	52 (18)
3	**Ni1**	16.08	1608	60 (95)	40 (17)
4	**Fe2**	8.65	865	41 (90)	59 (7)
5	**Co2**	9.14	915	53 (98)	47 (26)
6	**Ni2**	12.82	1282	54 (96)	46 (10)
7	**Fe3**	6.84	684	65 (93)	35 (19)
8	**Co3**	8.82	882	62 (93)	38 (15)
9	**Ni3**	9.95	995	61 (88)	39 (15)
10[d]	**Ni1**	nd	0	nd	nd
11[e]	**Ni1**	12.86	1286	32 (>99)	<1
12[e]	**Ni2**	10.48	1048	37 (76)	<1
13[e]	**Ni3**	7.21	721	5 (96)	<1

[a] Reaction conditions: complex, 10 μmol; solvent, chlorobenzene/toluene, 30 mL; temperature, 30 °C; time, 1 h; pressure, 10 bar; EtAlCl$_2$:Al/M = 250. [b] Determined using GC and n-heptane served as an internal standard. [c] Determined by GC and GC-MS. [d] Using the MMAO-12 co-catalyst. nd denotes not detected. [e] In toluene solvent, remaining products were alklytoluenes.

catalytic activity of 684 kg mol^{-1} h^{-1} compared to the catalytic activity of complex **Fe1** of 918 kg mol^{-1} h^{-1}. This may be linked to the degree of π-back-bonding abilities of the pyridyl group (**L1**) in comparison to the quinoline group (**L3**).[59] This trend agrees with the electronic effects observed in complexes **Fe1** and **Fe2**. In addition, the lower catalytic activities of the complexes **Fe3**, **Co3** and **Ni3** (anchored on the tridentate ligand **L3**$^-$) could be due to steric crowding. As an illustration, complexes **Fe3**, **Co3** and **Ni3** are six-coordinate, while those of anionic ligands **L1**$^-$ and **L2**$^-$ are four-coordinate. This has the overall effect of hindering ethylene coordination to the active metal site in the tridentate bound complexes, consistent with their diminished catalytic activities.[60]

The product distribution of the Fe(II), Ni(II) and Co(II) complexes was also driven by the structural variations in the complexes. Generally, Ni(II) complexes produced more C$_4$ oligomers than their Co(II) and Fe(II) counterparts. For example, the percentage compositions of C$_4$ oligomers of 60%, 48% and 39% were produced by **Ni1**, **Co1** and **Fe1** catalysts respectively (Table 2, entries 1–3). The nature of the coordinated ligand was also witnessed to control the product distribution. In general, the more sterically hindered complexes **Fe3**, **Co3** and **Ni3**

(ligated by tridentate **L3**$^-$), favoured the formation of C$_4$ oligomers, when compared to for instance complexes **Fe1**, **Co1** and **Ni1** supported on the less hindered **L1**$^-$ ligand (Table 2, entries 1–3 vs. 7–9). This trend agrees with the literature findings and fundamental concepts, where sterically hindered catalysts favour chain propagation over chain termination.[61,62] While there was no significant isomerism of the preformed C$_4$ fractions greater isomerism of the C$_6$ oligomers was observed. This is consistent with our previous reports and the proposed mechanism in Scheme S1 (ESI†).[63]

3.5. Density functional theory (DFT) studies

In attempts to gain in-depth understanding of the effects of the complex structure on the catalytic performance of these complexes in ethylene oligomerization reactions, we carried out density functional theory (DFT) computational studies on the structure–activity relationships of the complexes. The computational calculations were performed using the split basis set LANL2DZ (Los Alamos International 2 Double ζ) for Fe(II), Co(II) and Ni(II) complexes, and 6-311G(dp) for the remaining atoms.[33,35,36] The ground state electronic structures of the complexes (Fig. S36, ESI†) were employed to probe the effect of various global descriptors of the metal complexes on their catalytic performance in ethylene oligomerization reactions. First, the energy gaps were analysed to study their influence on the catalytic activities of the respective complexes (Table 3 and Fig. S37, ESI†). Two opposing trends were observed, controlled by the nature of the coordinated ligands (**L1**–**L3**$^-$). Comparison between the HOMO–LUMO energy gap and catalytic activities of the complexes (within a metal series) bearing the bidentate ligands (**L1**$^-$ and **L2**$^-$) reveal that the smaller the HOMO–LUMO energy gap, the higher the catalytic activity (Fig. S37, ESI†). For example, complexes **Fe1** and **Fe2** displayed HOMO–LUMO gaps of 0.1280 eV and 0.1289 eV, and catalytic activities of 918 kg mol^{-1} h^{-1} and 865 kg mol^{-1} h^{-1} respectively. This is consistent with the ethylene oligomerization reaction involving a nucleophilic attack to the metal centre by the ethylene monomer.[64] Thus smaller energy difference between the HOMO and LUMO should promote the coordination of the ethylene substrate to the metal centre. A similar observation was observed for **Co1**, **Co2**, **Ni1** and **Ni2** complexes (Fig. S37, ESI†). However, for complexes (**Fe3**, **Ni3** and **Co3**) anchored on the tridentate ligand **L3**, lower catalytic activities than, for example, **Fe1**, **Ni1** and **Co1** were reported despite lower HOMO–LUMO gaps. This points to

Table 3 Influence of global descriptors of the metal complexes on their catalytic activities in ethylene oligomerization reactions

Parameter	Fe1	Co1	Ni1	Fe2	Co2	Ni2	Fe3	Co3	Ni3
[a]HOMO-LUMO Energy Gap	0.1280	0.1259	0.1262	0.1289	0.1267	0.1281	0.1062	0.1036	0.1013
Global Softness	7.8113	7.9441	7.9221	7.7568	7.8959	7.8082	9.4127	9.6571	9.8707
Chemical Hardness	0.0640	0.0629	0.0631	0.0645	0.0633	0.0640	0.0531	0.0517	0.0507
NBO Charge	1.1730	1.0956	1.0438	1.1733	1.0960	1.0421	1.0846	1.0015	0.9293
Ionization Potential	0.2229	0.2222	0.2236	0.2217	0.2209	0.2230	0.2004	0.1979	0.1965
Chemical Potential	−0.1589	−0.1593	−0.1605	−0.1572	−0.1575	−0.1589	−0.1473	−0.1460	−0.1458
[b]Activity/Kg mol^{-1} h^{-1}	918	1036	1608	865	915	1282	684	882	995

[a] E_{LM} and E_{HM} are the LUMO and HOMO orbital energy values of the metal complexes and ethylene molecule, respectively. [b] Reaction conditions: complex, 10 μmol; solvent, chlorobenzene (30 mL), temperature, 30 °C; time, 1 h; pressure, 10 bar; EtAlCl$_2$, Al/M = 250.
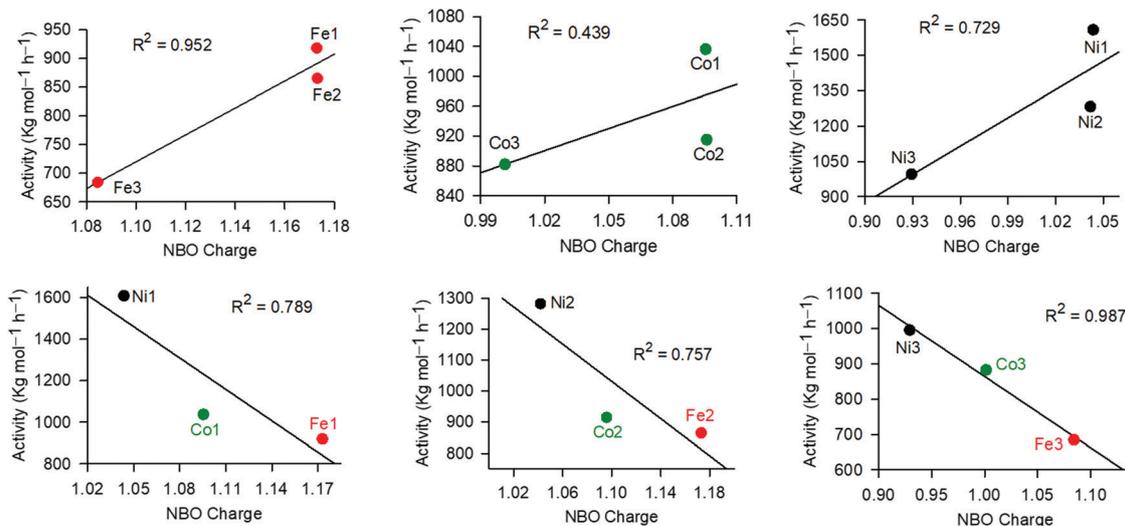
Fig. 4   Influence of the metal NBO charge on the catalytic activities of the complexes in ethylene oligomerization reactions.

structural effects being the major contributor here. For instance, complexes **Fe3**, **Co3** and **Ni3** of **L3** are six-coordinate and more sterically hindered, and thus limit facile coordination of the ethylene monomer. This argument is well supported by the results obtained for the global softness and hardness (Fig. S38, ESI†), where complexes **Fe3**, **Co3** and **Ni3** showed an opposite trend to the four-coordinate complexes.

In the ethylene oligomerization mechanism, coordination of the ethylene monomer to the metal active site is considered as the rate determining step and is largely controlled by the metal charge.[65] We thus used DFT studies to probe the possible role of the NBO charges of Fe, Ni and Co atoms in controlling the catalytic activities of these complexes (Table 3 and Fig. 4). From Fig. 4, the role of the coordinated ligand was evident within a

given metal series, where the higher the NBO charge, the higher the catalytic activity. For example, complexes **Ni1**, **Ni2** and **Ni3** carrying NBO charges of 1.044, 1.042 and 0.929, exhibited catalytic activities of 1608 kg mol^{-1} h^{-1}, 1282 kg mol^{-1} h^{-1} and 995 kg mol^{-1} h^{-1} respectively. A similar trend was reported for the Fe and Co catalysts (Fig. 4). Comparable NBO charges of the complexes anchored on ligands **L1** and **L2** is chemically sound since both the aldimine and ketimine units are remotely located from the metal atoms. On the other hand, the higher metal charges, on complexes supported on ligands **L1$^-$** and **L2$^-$**, in comparison to those of ligand **L3$^-$**, may be attributed to the pyridine ring being a better π-acceptor than the quinoline ring.[59,66] An opposite trend was interestingly observed on examinations of the different metal atoms, containing the
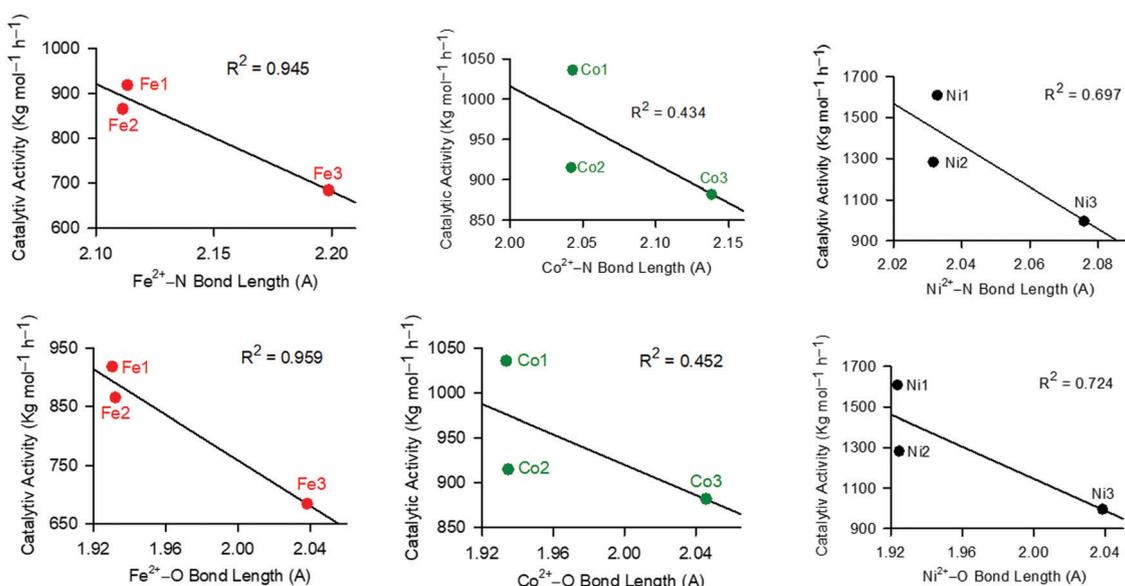

Fig. 5   The influence of the M−N/O bond length on the resultant catalytic activities of the complexes showing that higher bond lengths result in lower catalytic activities.

same ligand. For example, **Fe1**, **Ni1** and **Co1**, exhibited NBO charges of 1.173, 1.096 and 1.044 and catalytic activities of 918 kg mol^{-1} h^{-1}, 1036 kg mol^{-1} h^{-1} and 1608 kg mol^{-1} h^{-1}, respectively (Fig. 4). This could be assigned to the different charge/ionic size ratios, where the smaller Ni^{2+} has the highest charge/ionic size ratio, and hence was more susceptible to nucleophilic attack by the ethylene monomer.

Next, we investigated the possible role of ionization and chemical potentials of the complexes in ethylene oligomerization reactions. From the data presented in Fig. S39, (ESI†) all the complexes followed a similar trend, where the most negative complexes within the metal series (high tendency to lose an electron) were the most active. For example, the chemical potentials of **Ni1**, **Ni2** and **Ni3** complexes were −0.1605, −0.1589 and −0.1458, respectively (Table 3). This followed the order of their catalytic activities of 1608 kg mol^{-1} h^{-1}, 1282 kg mol^{-1} h^{-1} and 995 kg mol^{-1} h^{-1} respectively. A similar trend was observed for the other complexes and the ionization potential data (Fig. S39, ESI†). The negative chemical potential of the complexes is indicative of their relative stability. This is fundamentally reasonable since the less sterically crowded four coordinate complexes of ligands **L1**$^{-}$ and **L2**$^{-}$ are expected to be more stable than the six-coordinate complexes **Fe3**, **Ni3** and **Co3**.

We finally sort to understand the relationship between catalytic stability and activity, by analysing the dependence of catalytic activities on the M–N/O bond lengths (Fig. 5). A shorter bond length is associated with enhanced stability of the compounds, and *vice versa*. From Fig. 5, it was apparent that in all cases, longer bond lengths (M–N/O) were associated with decreased catalytic activities. This asserts the earlier data (chemical potential, hardness and softness), and points to the stability of the complexes as the driving force in controlling catalytic activities. Thus, longer bond distances led to the decomposition of the active species, consistent with the lower catalytic activities observed with the increase in M–N/O bond distances (Fig. 5).

4. Conclusions

Fe(ɪɪ), Co(ɪɪ) and Ni(ɪɪ) complexes of bidentate and tridentate (imino)phenol ligands bearing pyridine and quinoline motifs were successfully synthesized and characterized using IR and UV-visible spectroscopies, mass spectrometry, magnetic moment measurements, and micro-, and X-ray crystallography analyses. The solid-state structures of complexes **Fe3a** and **Ni3** confirmed the formation of six-coordinate bis(chelated) tridentate bound complexes. Experimental and theoretical UV-visible spectra were consistent with the presence of M(ɪɪ) oxidation state complexes in the bulk state. Activation of the Fe(ɪɪ), Co(ɪɪ) and Ni(ɪɪ) complexes with the EtAlCl$_2$ co-catalyst afforded active species in ethylene oligomerization reactions to give predominantly C$_4$ and C$_6$ oligomers. The catalytic activities and product distribution of the catalyst relied significantly on the complex structure. Theoretical DFT calculations point to the stability

and metal charge of the active species as the main factors controlling the resultant catalytic activities of the complexes.

Conflicts of interest

The authors declare no conflict of interest.

References

1 S. Damavandi, N. Samadieh, S. Ahmadjo, Z. Etemadinia and G. H. Zohuri, *J. Eur. Polym.*, 2015, **64**, 118–125.
2 A. P. R. Ehlert, E. M. Carvalho, D. Thiele, C. Favero, I. Vicente, K. B. Gusmao, R. Stieler, R. F. de Souza and M. O. de Souza, *Catal. Today*, 2017, **296**, 272–276.
3 A. Ghisolfi, C. Fliedel, V. Rosa, K. Y. Manakhov and P. Braunstein, *Organometallics*, 2014, **33**, 2523–2534.
4 W.-H. Sun, S. Jie, W. Zhang, Y. Song, H. Ma and J. Chen, *Organometallics*, 2006, **25**, 666–677.
5 W. Hang, Y. Weidong, J. Tao, L. Binbin, X. Wenqing, M. Jianjiang and H. Youliang, *J. Chin. Sci. Bull.*, 2002, **47**, 616.
6 K. P. Bryliakov and A. A. Antonov, *J. Organomet. Chem.*, 2018, **867**, 55–61.
7 L. Xiao, R. Gao, M. Zhang, Y. Li, X. Cao and W.-H. Sun, *Organometallics*, 2009, **28**, 2225–2233.
8 K. Kumar, T. Godeto and J. Darkwa, *J. Organomet. Chem.*, 2016, **818**, 137–144.
9 M. Brookhart, B. L. Small and A. M. A. Bennet, *J. Am. Chem. Soc.*, 1998, **120**, 4049–4054.
10 S. O. Ojwach, I. A. Guzei, L. L. Benade, S. F. Mapolie and J. Darkwa, *Organometallics*, 2009, **28**, 2127–2133.
11 G. M. Adams and A. S. Weller, *Coord. Chem. Rev.*, 2018, **355**, 150–172.
12 J. M. Benito, E. de Jesus, F. J. de La Mata, J. C. Flores, R. Gomez and P. Gomez-Sal, *Organometallics*, 2006, **25**, 3876–3887.
13 C. Bianchini, G. Giambastiani, I. G. Rios, G. Mantovani, A. Meli and M. A. Segarra, *Coord. Chem. Rev.*, 2006, **250**, 1391–1418.
14 M. Zada, L. Guo, R. Zhang, W. Zhang, Y. Ma, G. A. Solan, Y. Sun and W.-H. Sun, *Appl. Organomet. Chem.*, 2019, e4749.
15 R. Gao, W.-H. Sun and C. Redshaw, *Catal. Sci. Technol.*, 2013, **3**, 1172–1179.
16 Z. Wang, Q. Liu, G. A. Solan and W.-H. Sun, *Coord. Chem. Rev.*, 2017, **350**, 68–83.
17 Z. Wang, G. A. Solan, W. Zhang and W.-H. Sun, *Coord. Chem. Rev.*, 2018, **363**, 92–108.

18 P. Boulens, E. Pellier, E. Jeanneau, J. N. H. Reek, H. Olivier-Bourbigou and P.-A. R. Breuil, *Organometallics*, 2015, **34**, 1139–1142.

19 G. J. P. Britovsek, W. Keim, S. Mecking, D. Sainz and T. Wagner, *J. Am. Chem. Soc.*, 1993, **23**, 1632–1634.

20 M. O. de Souza, L. R. Rodrigues, R. M. Gauvin, F. R. de Souza, H. O. Pastore, L. Gengembre, J. A. C. Ruiz, J. M. R. Gallo, T. S. Milanes and M. A. Milani, *Catal. Commun.*, 2010, **11**, 597–600.

21 A. Tavman, I. Boz and A. Seher Birteksoz, *Spectrochim. Acta, Part A*, 2010, **77**, 199–206.

22 W. Yang, J. Yi, Z. Ma and W.-H. Sun, *Catal. Commun.*, 2017, **101**, 40–43.

23 M. K. Ainooson, S. O. Ojwach, I. A. Guzei, L. C. Spencer and J. Darkwa, *J. Organomet. Chem.*, 2011, **696**, 1528–1535.

24 O. S. Trofymchuk, D. V. Gutsulyak, C. Quintero, M. Parvez, C. G. Daniliuc, W. E. Piers and R. S. Rojas, *Organometallics*, 2013, **32**, 7323–7333.

25 H. Makio, H. Terao, A. Iwashita and T. Fujita, *Chem. Rev.*, 2011, **111**, 2363–2449.

26 Z. Sun, F. Huang, M. Qu, E. Yue, I. V. Oleynik, I. I. Oleynik, Y. Zeng, T. Liang, K. Li, W. Zhang and W.-H. Sun, *Rsc. Adv.*, 2015, **5**, 77913–77921.

27 S. Wang, W. Zhang, S. Du, S. Asuha, Z. Flisak and W.-H. Sun, *J. Organomet. Chem.*, 2015, **798**, 408–413.

28 M. Ngcobo and S. O. Ojwach, *J. Organomet. Chem.*, 2017, **846**, 33–39.

29 M. Ngcobo and S. O. Ojwach, *Inorg. Chim. Acta*, 2017, **467**, 1–5.

30 O. V. Dolomanov, L. J. Bourhis, R. J. Gildea, J. A. K. Howard and H. Puschmann, *J. Appl. Crystallogr.*, 2009, **42**, 339–341.

31 G. M. Sheldrick, *Acta Crystallogr., Sect. A: Found. Crystallogr.*, 2008, **64**, 339–341.

32 G. M. Sheldrick, *Acta Crystallogr., Sect. C: Struct. Chem.*, 2015, **12**, 3–8.

33 M. J. T. Frisch, G. W. Trucks, H. B. Schlegel, G. E. Scuseria, M. A. Robb, J. R. Cheeseman, G. Scalmani, V. Barone, B. Mennucci, G. A. Petersson, H. Nakatsuji, M. Caricato, X. Li, H. P. Hratchian, A. F. Izmaylov, J. Bloino, G. Zheng, J. L. Sonnenberg, M. Hada, M. Ehara, K. Toyota, R. Fukuda, J. Hasegawa, M. Ishida, T. Nakajima, Y. Honda, O. Kitao, H. Nakai, T. Vreven, J. A. Montgomery, Jr., J. E. Peralta, F. Ogliaro, M. Bearpark, J. J. Heyd, E. Brothers, K. N. Kudin, V. N. Staroverov, R. Kobayashi, J. Normand, K. Raghavachari, A. Rendell, J. C. Burant, S. S. Iyengar, J. Tomasi, M. Cossi, N. Rega, J. M. Millam, M. Klene, J. E. Knox, J. B. Cross, V. Bakken, C. Adamo, J. Jaramillo, R. Gomperts, R. E. Stratmann, O. Yazyev, A. J. Austin, R. Cammi, C. Pomelli, J. W. Ochterski, R. L. Martin, K. Morokuma, V. G. Zakrzewski, G. A. Voth, P. Salvador, J. J. Dannenberg, S. Dapprich, A. D. Daniels, O. Farkas, J. B. Foresman, J. V. Ortiz, J. Cioslowski and D. J. Fox, *Gaussian 16, Revision B.01*, Gaussian, Inc., Wallingford CT., 2016.

34 A. D. Becke, *Phys. Rev. B: Condens. Matter Mater. Phys.*, 1988, **A38**, 3098–3100.

35 A. D. Becke, *J. Chem. Phys.*, 1993, **98**, 5648–5652.

36 C. T. Lee, W. T. Yang and R. Parr, *Phys. Rev. B: Condens. Matter Mater. Phys.*, 1988, **37**, 785–789.

37 K. Rome and A. McIntyre, *Chromatogr. Today*, 2012, **52**, 52–55.

38 J. Wang, N. Zhang, C. Li, W. Shi and Z. Lin, *Adv. Polym. Technol.*, 2016, **35**, 21704–21712.

39 G. S. Nyamato, M. G. Alam, S. O. Ojwach and M. P. Akerman, *J. Organomet. Chem.*, 2015, **783**, 64–72.

40 F. A. Cotton, G. Wilkinson, C. A. Murillo and M. Bochmann, *Advanced Inorganic Chemisty*, Wiley, New York, 6th edn, 1999, p. 835.

41 P. W. Atkins, T. L. Overton, J. P. Rourke, M. T. Weller and F. A. Armstrong, *Inorganic Chemistry*, W. H. Freeman and Co., New York, 5th edn, 2010.

42 R. K. Chaggar, J. Fawcett and G. A. Solan, *Acta Crystallogr., Sect. E: Struct. Rep. Online*, 2003, **59**, 462–463.

43 L. Guo, X. Jing, S. Xiong, W. Liu, Y. Liu, Z. Liu and C. Chen, *Polymers*, 2016, **8**, 389–401.

44 K. Nienkemper, V. V. Kotov, G. Kehr, G. Erker and R. Fröhlich, *Eur. J. Inorg. Chem.*, 2006, 366–379.

45 P. Ghorai, A. Chakraborty, A. Panja, T. K. Mondal and A. Saha, *Rsc. Adv.*, 2016, **6**, 36020–36030.

46 P. Insiti, P. Jitthiang, P. Harding, K. Chainok, R. Chotima, J. Sirirak, S. Blackwood, A. Alkas, S. G. Telfer and D. J. Harding, *Polyhedron*, 2016, **114**, 242.

47 I. J. Bruno, J. C. Cole, P. R. Edgington, M. Kessler, C. F. Macrae, P. McCabe, J. Pearson and R. Taylor, *Acta Crystallogr., Sect. B: Struct. Sci.*, 2002, **58**, 389–397.

48 I. J. Bruno, J. C. Cole, P. R. Edgington, M. Kessler, C. F. Macrae, P. McCabe, J. Pearson, R. Taylor, I. R. Cooper, S. E. Harris and A. G. Orpen, *J. Chem. Inf. Comput. Sci.*, 2004, **44**, 2133–2144.

49 M. J. M. Chambell, *Coord. Chem. Rev.*, 1975, **15**, 279.

50 Diwaker, *Spectrochim. Acta, Part A*, 2014, **128**, 819–829.

51 M. M. Mostafa, A. E. Hammid, M. Shallaby and A. A. El-Asmy, *Trans. Mat. Chem.*, 1981, **6**, 303.

52 J. Ghannam, T. A. Assil, T. C. Pankratz, R. L. Lord, M. Zeller and W.-T. Lee, *Inorg. Chem.*, 2018, **57**, 8307–8316.

53 A. R. Karam, E. L. Catari, F. Lopez-Linares, F. Agrifoglio, G. Agrifoglio, C. L. Albano, A. Diaz-Barrios, T. E. Lehmann, S. V. Pekerar, L. A. Albornoz, R. Atencio, T. Gonzalez, H. B. Ortega and P. Joskowics, *Appl. Catal., A*, 2005, **280**, 165–173.

54 S. M. Nelana, K. Kumar, A. L. Guzei, T. Mahamo and J. Darkwa, *J. Organomet. Chem.*, 2017, **323**, 45–54.

55 J. Wang, S. Hou, L. Wang, H. Hou, N. Zhang and W. Shi, *Appl. Catal., A*, 2019, 55–61.

56 G. S. Nyamato, S. O. Ojwach and M. P. Akerman, *J. Mol. Catal. A: Chem.*, 2014, **394**, 274–282.

57 M. Ngcobo, G. S. Nyamato and S. O. Ojwach, *Mol. Catal.*, 2019, **478**, 110590.

58 J. Yu, X. Hu, Y. Zeng, L. Zhang, C. Ni, X. Hao and W.-H. Sun, *New J. Chem.*, 2011, **35**, 178–183.

59 G. A. Kinunda, *Tanz. J. Sci.*, 2018, **44**, 45–63.

60 G. E. Bekmukhamedov, A. V. Sukhov, A. M. Kuchaev and D. G. Yakhvarov, *Catalysts*, 2020, **10**, 498–518.

61 L. K. Johnson, S. Mecking and M. Brookhart, *J. Am. Chem. Soc.*, 1996, **118**, 267.

62 I. Pierro, G. Zanchin, E. Parisini, J. Marti-Rujas, M. Canetti, G. Ricci, F. Bertini and G. Leone, *Macromelecules*, 2018, **51**, 801–814.

63 M. Ngcobo and S. O. Ojwach, *Mol. Catal.*, 2021, **508**, 111583.

64 G. S. Nyamato, S. O. Ojwach and M. P. Akerman, *Dalton Trans.*, 2016, **45**, 3407–3416.

65 L. K. Johnson, C. M. Killian and M. Brookhart, *J. Am. Chem. Soc.*, 1995, **117**, 6414.

66 P. O. Ongoma and D. Jaganyi, *Dalton Trans.*, 2012, **44**, 10724–10730.